



Water Resources Research

RESEARCH ARTICLE

10.1002/2013WR015148

Key Points:

- Lattice Boltzmann simulation interfacial areas match experimental trends
- Wetting phase relative permeability is unaffected by wettability alteration
- Nonwetting phase relative permeability is decreased by wettability alteration

Correspondence to:

C. J. Landry,
chris.landry@beg.utexas.edu

Citation:

Landry, C. J., Z. T. Karpyn, and O. Ayala (2014), Relative permeability of homogenous-wet and mixed-wet porous media as determined by pore-scale lattice Boltzmann modeling, *Water Resour. Res.*, 50, 3672–3689, doi:10.1002/2013WR015148.

Received 4 DEC 2013

Accepted 8 APR 2014

Accepted article online 11 APR 2014

Published online 6 MAY 2014

Relative permeability of homogenous-wet and mixed-wet porous media as determined by pore-scale lattice Boltzmann modeling

C. J. Landry¹, Z. T. Karpyn², and O. Ayala^{3,4}

¹Bureau of Economic Geology, University of Texas at Austin, Austin, Texas, USA, ²John and Willie Leone Family Department of Energy and Mineral Engineering, and EMS Energy Institute, Pennsylvania State University, University Park, Pennsylvania, USA, ³Department of Engineering Technology, Old Dominion University, Norfolk, Virginia, USA, ⁴Centro de Métodos Numéricos en Ingeniería, Escuela de Ingeniería y Ciencias Aplicadas, Universidad de Oriente, Puerto La Cruz, Venezuela

Abstract We present a pore-scale study of two-phase relative permeability in homogenous-wet porous media, and porous media altered to a mixed-wet state. A Shan-Chen type multicomponent lattice Boltzmann (LB) model is employed to determine pore-scale fluid distributions and relative permeability. Mixed-wet states are created by altering the wettability of solid surfaces in contact with the nonwetting phase at the end of steady state simulation of initially homogenous-wet porous media. To ensure accurate representation of fluid-solid interfacial areas, we compare LB simulation results to experimental measurements of interfacial fluid-fluid and fluid-solid areas determined by X-ray computed microtomography imaging of water and oil distributions in bead packs. The LB simulations are found to match experimental trends observed for fluid-fluid and fluid-solid interfacial area-saturation relationships. The relative permeability of both fluids in the homogenous-wet porous media was found to decrease with a decreasing contact angle. The relative permeability of both fluids in the altered, mixed-wet porous media was found to decrease for all mixed-wet states in comparison to the initial homogenous-wet states. The nonwetting phase relative permeability decreased significantly, while the wetting phase experienced only a minor decrease. The significance of the decrease was found to be dependent on the distribution of the unaltered solid surfaces, with less dependence on the severity of alteration.

1. Introduction

Macroscale multiphase flow properties of porous media (i.e., relative permeability and capillary pressure) are strongly dependent on wettability. The wettability of a porous medium is initially determined by its mineral composition. However, brines and oils can alter the wettability of porous media, such that the multiphase flow properties of a rock can be significantly dependent on saturation history. Subsequently, the majority of consolidated and unconsolidated porous media have a mixed or fractional wettability, particularly those that have been exposed to both brines and oils.

Wettability is conventionally measured using the Amott-Harvey method or the U.S. Bureau of Mines (USBM) method. Both are bulk measurements that determine an index of wettability from displacement experiments. Indices range from -1 to 1 for perfectly oil-wet to perfectly water-wet conditions, and do not distinguish between homogenous-wet and mixed-wet porous media (e.g., a homogenous neutrally wet porous medium and one with 50/50 mixed-wet porous medium). At the pore scale, wettability is described by contact angles. The contact angle is measured through the aqueous phase and ranges from 0° to 180° , for perfectly water-wet to perfectly oil-wet, respectively. Thus, each individual mineral constituent of a natural porous media can be independently described by a contact angle, and a wide variety of mixed-wet states can be considered. Common reservoir porous media include siliclastic rocks (i.e., sandstone) primarily composed of quartz, but also containing significant amounts of feldspars, calcite, dolomite and clays, and carbonate rocks (i.e., limestone) composed primarily of calcite, dolomite, clays, and organics. All of these mineral constituents are candidates for wettability alteration.

Once a fluid is in contact with a mineral surface in porous media, the alteration in wettability is controlled by fluid-mineral surface chemistry. As summarized by Buckley and Liu [1998], the mechanisms involved in

crude oil/brine/solid interaction include polar interactions between the polar functional groups in the oil and polar surface sites on the mineral, surface precipitation, acid/base reactions, and ion binding. One of the most often encountered mechanisms of wettability alteration by crude oils is the adsorption and deposition of asphaltenes on mineral surfaces. Asphaltenes can render initially water-wet mineral surfaces oil-wet. *Saraji et al.* [2010] measured the adsorption of asphaltene to calcite, dolomite, and quartz by asphaltene-containing oils under flow conditions. The asphaltene was found to adsorb the most to calcite, and to a lesser extent quartz and dolomite. Wettability was not measured, but it was concluded that the amount of asphaltene adsorbed was sufficient to form a monolayer on all minerals.

Conventional measurement of oil recovery and macroscale flow properties from mixed-wet reservoir rock cores demonstrates some of the important trends observed in field-scale variations of saturation history and wettability. *Jadhunandan and Morrow* [1995] investigated changes in wettability and oil recovery from Berea cores aged with two different crude oils and varying initial water saturations (S_{wi}), aging temperatures, and brine compositions. Regardless of oil type and brine composition, the Amott index of the rock increased monotonically with S_{wi} . *Jerauld and Rathmell* [1997] observed the same trend in oil-wetness and connate water saturation for Prudhoe Bay sandstone cores composed primarily of quartz. Core wettability trended more oil-wet with decreasing connate water saturation above the oil-water contact line of the reservoir. With more oil present in the rock, a larger fraction of the pore space will be in contact with the oil, resulting in a larger surface area of the pore space subject to wettability alteration.

There are two factors to consider in the study of wettability alteration, the chemistry of alteration and the distribution of fluids in the pore geometry with respect to mineral constituents of the porous media. There are only a limited number of studies that have attempted to measure contact angles at the pore scale within natural porous media, where mineral heterogeneity exists in individual pores. *Robin et al.* [1995] imaged the distribution of oil and water phases in a reservoir sandstone and carbonate before and after wettability alteration using cryogenic scanning electron microscopy. The images provided qualitative evidence of individual mineral wettability alteration within individual pores. Many of the trends in mineral wettability alteration discussed above are found in these images. Although these types of images confirm the assumptions of bulk studies, they do not provide much insight into the 3-D pore geometry that governs the movement of fluids. To obtain 3-D images nondestructive 3-D imaging of pore geometry and fluid distributions using X-ray computed microtomography (CMT) has become a popular tool to image and analyze pore geometries and fluid distributions in these pore spaces. Many investigators have used CMT to image a variety of fluid distributions in unconsolidated materials [*Culligan et al.*, 2006; *Brusseau et al.*, 2006, 2008; *Constanza-Robinson et al.*, 2008; *Al-Raoush*, 2009; *Lebedeva and Fogden*, 2011] and rock [*Coles et al.*, 1998; *Turner et al.*, 2004; *Prodanovic et al.*, 2007; *Iglauer et al.*, 2011; *Silin et al.*, 2011; *Kumar et al.*, 2012]. Armed with knowledge of the fluid/mineral wettability alteration and pore geometry, pore-scale models can be employed to investigate the macroscale multiphase flow properties of mixed-wet porous media.

The focus of this paper is to further elucidate the relationship between mixed-wet states and relative permeability. In the past two decades, pore-network models have been used to model wettability alteration [*Blunt*, 1997; *Dixit et al.*, 1998, 1999; *Blunt et al.*, 2002; *Jackson et al.*, 2003; *Al-Futaisi and Patzek*, 2004; *Hoiland et al.*, 2007; *Zhao et al.*, 2010], and match experimental measurements of relative permeability of natural porous media [*Oren et al.*, 1998; *Blunt et al.*, 2002; *Jackson et al.*, 2003; *Al-Futaisi and Patzek*, 2004]. *Kovscek et al.* [1993] introduced a physically based model for wettability alteration within individual pores; each pore is represented by a capillary tube with a star-shape cross-section. The tube is initially occupied by the wetting phase; during drainage the wetting phase is displaced by a piston-like mechanism by the nonwetting phase. The nonwetting phase will now occupy the center of the pore, leaving the corners occupied by the wetting phase. For the surface of the pore to make contact with the nonwetting phase, the capillary pressure must overcome a critical capillary pressure at which the wetting film destabilizes to molecular thickness. Once contact is made, the wettability of the surface of the pore in contact with the oil is altered. This concept was further extended to squares [*Blunt*, 1997], polygons [*Hui and Blunt*, 2000], triangles and lenses [*Oren et al.*, 1998]. As is noted in *Blunt* [1997], the critical capillary pressure for film destabilization is not known for each individual pore; pore-network models cope with this by assigning a wettability alteration to a fraction of the pores occupied by oil. These fractions can then be varied to observe resulting multiphase flow behavior. For pore-network modeling of mixed-wet media, there are three general possible modes of assigning fractional wettability to pores—the largest pores, the smallest pores, or at random [*Dixit*

et al., 1999; *Hoiland et al.*, 2007]. The choice of contact angles representing the wettability can also be uniform or distributed at random over a range. With these free parameters, a large variety of mixed-wet states can be modeled. There are concerns regarding the use of pore-network models for the study of wettability alteration and its effect on multiphase flows. Representative pore networks can be extracted from 3-D images of pore spaces, either from process-based model representations of porous media [*Oren et al.*, 1998; *Oren and Bakke*, 2003] or from CMT images [*Hazlett*, 1995; *Prodanovic et al.*, 2006]. However, the simplification of the pore space into capillary tubes of varying shape is not predisposed to the inclusion of knowledge of the mineral composition of the pores, particularly when individual pores and throats are bounded by more than one mineral. The surface chemistry of wettability alteration is highly dependent on accurate representation of fluid/mineral interfacial areas, which may be difficult to model without proper inclusion of the mineral composition of pores.

In this paper, we use a more rigorous pore-scale modeling approach. The lattice Boltzmann (LB) method can directly use 3-D images of pore space by a one-to-one correlation of image voxels to lattice sites. The accurate representation of any pore geometry is then only a question of image and lattice resolution. This makes the model very appealing over pore-network models. However, it is far more computationally expensive, requiring in the order of 10^{4-5} more CPU time than an equivalent pore-network model [*Vogel et al.*, 2005]. The computational needs of LB are compensated by its inherent parallelism—in most models each node is only aware of its neighboring nodes. Multiphase LB models have been validated against experimental measurements of capillary pressure in bead packs [*Pan et al.*, 2004; *Schaap et al.*, 2007; *Porter et al.*, 2009] and sandstones [*Ramstad et al.*, 2010, 2012], as well as experimental measurements of relative permeability in sphere packs [*Hao and Cheng*, 2010; *Ghassemi and Pak*, 2011] and sandstones [*Ramstad et al.*, 2010, 2012]. Investigation of mixed-wet porous rock using LB is limited to the work of *Hazlett et al.* [1998], but it has been applied in a more recent study of mixed-wet porous media in fuel-cells [*Mukherjee et al.*, 2009]. In *Hazlett et al.* [1998], a CMT image of a reservoir sandstone was translated directly into a lattice for LB multiphase displacement simulations for a strongly water-wet sandstone and a mixed-wet sandstone. The mixed-wet state was determined by simulating drainage to irreducible water saturation. At the end of the drainage, the pore walls in contact with the nonwetting phase are altered in wettability. In comparison to the originally homogenous-wet state, the mixed-wet state showed a significant decrease in the nonwetting phase relative permeability, and an insignificant change in the wetting phase relative permeability. This suggests that the nonwetting phase permeability is generally less for a mixed-wet state over a homogenous-wet state. Although there has been a fair amount of validation of LB methods via matching experimental measurements of macroscale flow properties, few have compared fluid distributions imaged using CMT with LB model results. *Sukop et al.* [2008] compared two phase fluid distributions in a sand pack imaged using CMT to distributions resulting from LB simulations. The saturation per slice was found to match experimental results well, but there was no analysis presented of interfacial area measurements. *Porter et al.* [2009] compared interfacial fluid-fluid areas measured by CMT to LB displacement simulations and found a good match for drainage simulations in bead packs.

Our objective is to investigate the sensitivity of relative permeability to wettability alteration as a result of saturation history and the initial state of wettability. Proper pore-scale simulations of wettability alteration require accurate predictions of fluid-solid interfacial areas. To test the ability of the LB model to predict these interfacial areas, we will first compare experimental measurements determined by CMT images of oil/brine fluid distributions in water-wet and weakly oil-wet bead packs from *Landry et al.* [2011] to the results of LB simulations. The bead packs can be viewed as simple analogs of water-wet siliclastic porous media and weakly oil-wet carbonate porous media. There are three variables of interest in our investigation of relative permeability—saturation relationships and their dependence on wettability, the initial wetting state of the porous media, the saturation at which wettability alteration takes place, and the severity of alteration. As was done in the work of *Hazlett et al.* [1998], the wettability of solid surfaces in contact with the nonwetting fluid, after fluid distribution is established by homogenous-wet LB simulations, will be altered to create a mixed-wet porous medium. Relative permeability measurements on the initial and mixed-wet states will then be carried out using the LB model. We will be able to evaluate the extent to which the LB model can recreate pore-scale distributions of immiscible fluids, and compare relative permeability measurements of mixed-wet states. In this simplified scenario, the initial wettability, saturation of alteration, and severity of alteration control the mixed-wet state of the porous media. The only variable in our simulations is

wettability, as a result of these three parameters. Natural porous media is subject to a far more complex wettability alteration process, dependent on numerous variables related to the mineral-fluid interactions. However, the resulting evolution of relative permeability—saturation relationships can be investigated without such considerations.

2. Materials and Methods

2.1. Experimental Measurements

The validation of pore-scale models at the pore scale is limited in the literature. Here we compare LB simulation results to CMT images of brine/oil distributions in strongly water-wet (glass) and weakly oil-wet (polyethylene) bead packs from Landry *et al.* [2011]. Both bead types were spherical with a size range between 0.425 and 0.600 mm, and packed in a column 25.4 mm in diameter and ~80–90 mm in length. The fluids used were a 4–8% NaI brine and kerosene, with dynamic viscosities of 1.00 and 2.43 cP, respectively. The bead packs were initially fully saturated with brine, followed by capillary-dominated displacement by kerosene, then brine. At the end of each displacement, CMT images were taken with a voxel resolution of $0.0260 \times 0.0260 \times 0.0292 \text{ mm}^3$ and $0.0259 \times 0.0259 \times 0.0274 \text{ mm}^3$, for the glass and polyethylene bead packs, respectively. Due to the relatively large pore radius of these porous media, gravity plays a significant role in the distribution of fluids in these bead packs. This results in a classic capillary transition-zone saturation profile in both bead packs at the end of drainage, from which fluid distributions can be observed at varying fluid saturations. From these images, specific interfacial fluid areas were measured. Due to the limited resolution of CMT images, the specific interfacial areas measured in Landry *et al.* [2011] do not account for interfacial areas between thin wetting films and the nonwetting phase/solid. Thus, the specific fluid-fluid interfacial areas and specific fluid-solid areas used for comparison here do not include these films. For more information regarding these measurements, please refer to Landry *et al.* [2011]. These measurements of volume and area will be compared in this investigation to the results of LB simulations.

2.2. Single-Phase BGK Lattice Boltzmann Model

The LB method is a mesoscopic method based on microscopic particle dynamics that provides numerical solutions to macroscopic hydrodynamics. In short, fluids are modeled as swarms of streaming and colliding particles. Each node on the lattice contains a particle distribution function, $f_i(\mathbf{x}, t)$, where i is the index of each discrete velocity, \mathbf{x} is the location of the node on the lattice, and t is time; here we use a D3Q19 lattice [Qian *et al.*, 1992]. The D3Q19 particle distribution function has 19 discrete velocities, \mathbf{e}_i , including a zero velocity and 18 velocities pointing to neighboring nodes. The particle distribution function is also referred to as the density function—the macroscopic density at each node is represented by a distribution of densities of particles moving along each discrete velocity. The particle distribution function evolves in time according to the discrete lattice Boltzmann equation,

$$f_i(\mathbf{x}, t) - f_i(\mathbf{x} + \mathbf{e}_i \Delta t, t + \Delta t) = \frac{\Delta t}{\tau} [f_i(\mathbf{x}, t) - f_i^{eq}(\mathbf{x}, t)], \quad (1)$$

where τ is the relaxation parameter, Δt is a discrete time step ($\Delta t = 1$, for one time iteration, in lattice units, 1 tu), and $f_i^{eq}(\mathbf{x}, t)$ is the equilibrium particle distribution function. The left-hand side of the equation represents the streaming of particles by passing the particle distribution at each discrete velocity to the respective neighboring node. The right-hand side of the equation represents the collision of particles as a partial relaxation to the equilibrium particle distribution. The relaxation parameter τ (also known as the collision interval) is representative of the rate of particle collisions, and is related to the kinematic viscosity, ν , of the lattice by, $\nu = c_s^2(\tau - 1/2)$, where c_s is the speed of sound of the lattice, or propagation speed, equal to $c/\sqrt{3}$. The discrete lattice speed unit $c = \Delta t/\Delta x$ is the ratio of the lattice spacing ($\Delta x = 1$ lattice length unit, lu) and the time step. Here we use Bhatnagar-Gross-Krook (BGK) dynamics, meaning the relaxation parameter is defined by a single value. The D3Q19 equilibrium particle distribution function $f_i^{eq}(\mathbf{x}, t)$ can be calculated as

$$f_i^{eq}(\mathbf{x}, t) = w_i \rho \left[1 + \frac{\mathbf{e}_i \cdot \mathbf{u}^{eq}}{c_s^2} + \frac{(\mathbf{e}_i \cdot \mathbf{u}^{eq})^2}{2c_s^4} - \frac{\mathbf{u}^{eq} \cdot \mathbf{u}^{eq}}{2c_s^2} \right], \quad (2)$$

where w_i is the weight of each discrete velocity, ρ is the density of $f_i(\mathbf{x}, t)$, and \mathbf{u}^{eq} ($\mathbf{u}^{eq} = [u_x \ u_y \ u_z]$) is the macroscopic velocity moment of $f_i(\mathbf{x}, t)$. The discrete velocities \mathbf{e}_i are defined as follows,

$$=c \begin{bmatrix} 0 & 1 & -1 & 0 & 0 & 0 & 0 & 1 & 1 & -1 & -1 & 1 & -1 & 1 & -1 & 0 & 0 & 0 & 0 \\ 0 & 0 & 0 & 1 & -1 & 0 & 0 & 1 & -1 & 1 & -1 & 0 & 0 & 0 & 0 & 1 & 1 & -1 & -1 \\ 0 & 0 & 0 & 0 & 0 & 1 & -1 & 0 & 0 & 0 & 0 & 1 & 1 & -1 & -1 & 1 & -1 & 1 & -1 \end{bmatrix} \quad (3)$$

with weights $w_i = 1/3 (i=1)$, $w_i = 1/18 (i=2, 3, \dots, 7)$, $w_i = 1/36 (i=8, 9, \dots, 19)$. The density is obtained by summing the particle densities, $\rho = \sum_i f_i$, and the macroscopic velocity is obtained by summing the particle momentum and dividing by density, $\mathbf{u} = (\sum_i f_i \mathbf{e}_i) / \rho$. To impose external forces, \mathbf{F}_{ext} , momentum is added to the macroscopic velocity in the following way,

$$\mathbf{u}^{\text{eq}} = \mathbf{u} + \frac{\mathbf{F}_{\text{ext}} \tau}{\rho}, \quad (4)$$

where \mathbf{u} is the macroscopic velocity calculated from the particle distribution function prior to collision. Each time iteration of the LB equation proceeds in three steps. First, the particle distributions are streamed to respective nodes. Second, the macroscopic density and velocity are determined from these new particle distributions, and when present, with the inclusion of an exterior force as stated above. Third, the equilibrium particle distribution is obtained and the particle distribution undergoes collision. There are three types of lattice nodes: fluid nodes, bounce-back nodes, and solid nodes. The nodes on which fluids move are fluid nodes, the nodes on the surface of solids are bounce-back nodes, and nodes on which no fluids exist are solid nodes (these nodes are ignored). The bounce-back nodes act as algorithmic devices that return incoming streamed particle densities with the opposite momentum, producing a no-slip condition halfway between the fluid and bounce-back node [He et al., 1997].

2.3. Shan-Chen Multicomponent Lattice Boltzmann Model

We employ the Shan-Chen multicomponent (SC-MC) LB model to simulate two-phase immiscible fluid flow [Shan and Chen, 1993, 1994; Martys and Chen, 1996]. The SC-MC LB model is one of the least computationally demanding multiphase LB models, and for this reason one of the most commonly used multiphase LB models. Two immiscible fluids are simulated on the lattice by representing each fluid phase with its own particle distribution function, $f_i^\sigma(\mathbf{x}, t)$, where $\sigma = w, nw$ is the index for each component particle distribution function in a two-phase system. The component particle distribution interact via a pseudopotential interparticle force ($\mathbf{F}_{p,\sigma}$) defined as,

$$\mathbf{F}_{p,\sigma}(\mathbf{x}, t) = -G_c \rho_\sigma(\mathbf{x}, t) \sum_i w_i \rho_\sigma(\mathbf{x} + \mathbf{e}_i \Delta t, t) \mathbf{e}_i, \quad (5)$$

where G_c is the parameter controlling the strength of the interparticle force, when G_c is positive the force is repulsive. Only the nearest-neighbor nodes are considered in the calculation of the interparticle force. The adhesion force between fluids and solid surfaces is imposed with the addition of an adsorption coefficient, $G_{ads,\sigma}$, on bounce-back nodes,

$$\mathbf{F}_{ads,\sigma}(\mathbf{x}, t) = -G_{ads,\sigma} \rho_\sigma(\mathbf{x}, t) \sum_i w_i s(\mathbf{x} + \mathbf{e}_i \Delta t, t) \mathbf{e}_i \quad (6)$$

where s is an indicator function that denotes the existence of a bounce-back node, as in, $s(\mathbf{x} + \mathbf{e}_i \Delta t, t) = 1$ when $\mathbf{x} + \mathbf{e}_i \Delta t$ is occupied by a bounce-back node. Following the recommendations of Huang et al. [2007], negative values of $G_{ads,\sigma}$ are used for wetting fluids and positive values of $G_{ads,\sigma}$ are used for the nonwetting fluids, with $G_{ads,nw} = -G_{ads,w}$. The adsorption coefficients create an adhesion force that determines the wettability of the solid surface. These forces are included in the lattice Boltzmann equation in the same manner as the exterior force,

$$\mathbf{u}_\sigma^{\text{eq}} = \mathbf{u} + \frac{(\mathbf{F}_{ads,\sigma} + \mathbf{F}_{p,\sigma} + \mathbf{F}_{\text{ext},\sigma}) \tau_\sigma}{\rho_\sigma}, \quad (7)$$

where the common velocity for the fluids is,

$$\mathbf{u}' = \frac{\sum_{\sigma} \left(\sum_i \frac{f_i^{\sigma} \mathbf{e}_i}{\tau_{\sigma}} \right)}{\sum_{\sigma} \frac{\rho_{\sigma}}{\tau_{\sigma}}}. \quad (8)$$

The adsorption coefficients ($G_{ads,w}$, $G_{ads,nw}$) in a Shan-Chen D3Q19 two-component system (wetting and nonwetting fluids) can be estimated for a given contact angle by the following equation proposed by Huang *et al.* [2007],

$$\cos \theta_w = \frac{G_{ads,nw} - G_{ads,w}}{G_c \frac{\rho_w - \rho_{nw/w}}{2}}, \quad (9)$$

where ρ_w is the density of the wetting fluid and $\rho_{nw/w}$ is the dissolved density of the nonwetting fluid in the wetting fluid (for values of G_c sufficient to segregate multiple components the dissolved density is very low). The lattice pressure at each node is determined by the D3Q19 Shan-Chen MC LB model equation of state,

$$P = \frac{1}{3} [\rho_w + \rho_{nw}] + \frac{1}{3} [G_c \rho_w \rho_{nw}] \quad (10)$$

All LB simulations presented here were executed using the open source code Palabos version 1.0.

2.4. LB Model Implementation

There are a collection of parameters that are chosen by the user to define a LB model simulation of fluid flow. The resolution of the lattice is an important factor when designing a LB simulation, optimally the resolution should be as fine as computing resources allow. However, due to the immense computational demand of LB simulations it is often the case that computing resource limits and time constrictions determine the resolutions of LB fluid flow simulations in porous media. Also, the necessary resolution to adequately represent flow in a porous medium is dependent on the pore structure, thus determining an adequate resolution for simulations merits further investigation. Given our computing resources, we chose to translate our CMT images with a 1-to-1 correlation, voxel-to-node. This ensures we are using a resolution great enough to capture the fluid-fluid and fluid-solid interfacial areas measured by CMT, and results in lattice sizes within the limits of our computing resources. The imaged voxel resolution of the glass bead pack is $0.0260 \times 0.0260 \times 0.0292 \text{ mm}^3$; to impose a 1-to-1 correlation of voxel-to-node, the raw image of the pore geometry is resampled to $0.0260 \times 0.0260 \times 0.0260 \text{ mm}^3$ and segmented into pore and solid voxels. The pore voxels of the segmented image volume are translated as fluid nodes, and the solid voxels that are in contact with pore voxels are translated as bounce-back nodes, with all other solid voxels being ignored in the lattice (Figure 1). The resolution of the imaged voxels determines the physical size of a lattice length unit, lu , here being the side length of a CMT voxel, and the physical mass of lattice mass unit, mu , being the product of the volume of a CMT voxel and the density of the physical fluid being simulated.

Throughout the LB simulations presented here, the global sum of the lattice density of the fluids, $\rho = \rho_w + \rho_{nw}$, is set to $1.0 \text{ mu}/lu^3$. Other parameters control the viscosity ratio of the fluids and the wettability of the solid surfaces. The time relaxation parameter is set to 1 for both fluids; the purpose of this being two-fold. The relaxation parameter determines the viscosity of each fluid, and thus the viscosity ratio of the fluids. Our experimental fluids are kerosene and water with a viscosity ratio, $M = \mu_{nw}/\mu_w$, of 2.3 and 0.43 for the glass bead pack and polyethylene bead pack (Note: in the glass bead pack the kerosene is the nonwetting phase, in the polyethylene bead pack the water is the nonwetting phase) displacements, respectively. The capillary number, N_{Ca} , is a dimensionless measure of the ratio of viscous to capillary forces, and is defined as, $N_{Ca} = \mu u / \gamma$, where μ is the dynamic viscosity, u is the fluid velocity in the direction of flow, and γ is the interfacial tension. The capillary number of the experimental displacements was very low, on the order of $N_{Ca} = 10^{-7}$. Given the capillary forces are so much greater than the viscous forces; we assume simulating fluids with a viscosity ratio of 1 will suffice for our needs. Also the use of BGK dynamics has been shown to result in viscosity-dependent permeability outside time-relaxation parameters of 1 [Pan *et al.*, 2006]. A time relaxation parameter of 1 minimizes systematic model errors and is representative of the

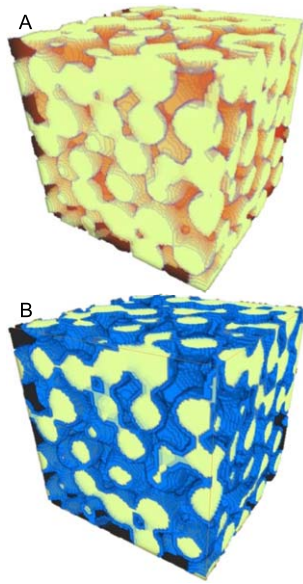


Figure 1. (a) Segmented CMT image of the bead pack with solid voxels colored white and (b) the corresponding lattice of the LB model with the bounce-back nodes in blue.

interfacial areas determined by LB simulations to experimental CMT measurements. As previously mentioned and illustrated in Figure 1, a 1-to-1 correlation of CMT voxel to lattice node is used. The image chosen was 100^3 voxel³, or ~ 5 beads to a side. Larger lattices up to 200^3 voxel³ were also used in initial simulations, but the results were similar to results using the smaller 100^3 voxel³ lattices at 1/8 of the computational cost. The simulation volume is bounded by walls orthogonal to the direction of flow; the increase in the solid surface area from these walls is negligible. In our steady state simulations, the initial density of each fluid is uniformly set at a desired saturation with a sum of 1, $\rho_w + \rho_{nw} = 1.0$, and an exterior force of $\mathbf{F}_{\text{ext},\sigma} = 0.00001$ is applied to both fluids in the direction of flow resulting in capillary-dominated flow ($N_{Ca} \approx 10^{-5}$). This setup allows the fluids to segregate without further input from the user. The disadvantage of this setup is it allows fluids access to pores that may not be accessible in displacement processes, leading to a more scattered nonwetting fluid distribution than what would be observed experimentally.

To compare the fluid distributions of the LB simulation to experimental images, we measure the specific fluid surface areas and specific interfacial areas. For details on the experimental measurement of these areas refer to Landry *et al.* [2011]. To measure these areas and volumes of fluids from the LB results, the lattice must be first segmented to identify the fluid occupying each node, here the fluid occupying the node, $\varphi_\sigma(\mathbf{x})$, is defined as the fluid with the greatest density,

$$\rho_\sigma(\mathbf{x}) > \rho_{\bar{\sigma}}(\mathbf{x}) \rightarrow \varphi_\sigma(\mathbf{x}) = 1 \quad (11)$$

The volume of the fluid is,

$$V_\sigma = \sum_{\mathbf{x}} \Delta x^3 \varphi_\sigma(\mathbf{x}) \quad (12)$$

where $\Delta x^3 = 0.026000^3$ mm³. The volume of the solid is simply the remainder of the lattice not occupied by fluid nodes, $V_s = V_{\text{bulk}} - V_w - V_{nw}$, where V_{bulk} is the volume of the whole lattice. The wetting-phase, nonwetting phase, and solid surface areas, A_δ , where $\delta = w, nw, s$, are measured using a modified marching cubes algorithm, this algorithm wraps a triangular mesh around the segmented data [Dalla *et al.*, 2002]. The specific fluid and solid surface areas, α_δ , are defined as, $\alpha_\delta = A_\delta / V_{\text{bulk}}$. The specific solid surface area of the lattice, $\alpha_s = 5.664$ mm⁻¹, falls within the small range of varying specific solid surface areas measured experimentally in Landry *et al.* [2011] (measurements were taken from different parts of the bead pack and had slightly

physical system to be modeled. The interfacial tension of the lattice is determined by the value of G_c , we use a value of 1.8, as suggested by Huang *et al.* [2007], giving a lattice interfacial tension of 0.100. In the SC-MC LB model, values of G_c lower than 1.8 decrease the contrast of the fluids, while higher values result in an undesirable compression of fluids [Schaap *et al.*, 2007; Huang *et al.*, 2007]. As was previously mentioned, the desired contact angle can be determined by the equation proposed by Huang *et al.* [2007] for given adsorption coefficients $G_{\text{ads},w}$ and $G_{\text{ads},nw}$. We do not know exactly what the contact angles are in our experimental system, we are only aware of the fact that the glass bead pack is water-wet and the polyethylene bead pack is weakly oil-wet. To compare LB results to experimental results we will simulate a range of contact angles.

3. Results

3.1. Fluid-Fluid and Fluid-Solid Interfacial Areas

The objective of this investigation is to study flow in mixed-wet porous media. The mixed-wet states are a result of wettability alteration at nonwetting phase-solid interfaces as determined by homogenous-wet LB simulations. Therefore, it is important that the model can accurately predict the interfacial areas between solids and fluids. To validate our method, we compare the fluid surface and

different specific solid surface areas), and should not significantly impact comparisons between the model and experimental measurements.

We are interested in comparing three specific interfacial areas, the specific fluid-fluid interfacial area, the nonwetting fluid-solid interfacial area, and the wetting fluid-solid interfacial area. The specific fluid-fluid interfacial area is the total area of the fluid-fluid interfaces (meniscus) normalized to bulk volume and is defined as [Dalla *et al.*, 2002],

$$\alpha_i = \frac{1}{2}(\alpha_w + \alpha_{nw} - \alpha_s). \quad (13)$$

The specific fluid-fluid interfacial area is important to the study of multiphase flows; it is here that energy and mass are transferred between fluid phases. The specific wetting phase-solid interfacial area, α_{ws} , and the specific nonwetting phase-solid interfacial area, α_{nws} , are defined as, $\alpha_{\sigma s} = \alpha_{\sigma} - \alpha_i$. The solid surface area varies in the experimental images, therefore we normalize the specific fluid-solid interfacial areas to the specific solid surface area, giving us the fractional wetting fluid-solid interfacial area, χ_{ws} , and the fractional nonwetting fluid-solid interfacial area, χ_{nws} , defined as,

$$\chi_{\sigma s} = (\alpha_{\sigma} - \alpha_i) / \alpha_s. \quad (14)$$

The wettability alteration that will be investigated here will occur on bounce-back nodes in contact with the nonwetting phase, and the fraction of the surface that will be altered is equal to the fractional nonwetting fluid-solid interfacial area. Four contact angles are considered, $\theta \approx 77^\circ$, 63° , 48° , 27° , resulting from setting $G_{ads,\sigma} = \pm 0.1$, ± 0.2 , ± 0.3 , ± 0.4 , respectively. A comparison of LB and experimental measurements of specific fluid-fluid interfacial areas can be found in Figure 2. Qualitatively, the LB simulations show a distinctive curve trending toward a maximum at wetting phase saturations between 0.3 and 0.5. This same curve is observed in the experimental measurements from the glass and polyethylene bead packs, and has also been reported by both previous experimental and numerical investigations [Reeves and Celia, 1996; Culligan *et al.*, 2006; Brusseau *et al.*, 2006; Schaap *et al.*, 2007; Joekar-Niasar *et al.*, 2008; Landry *et al.*, 2011]. We also observe an increase in specific fluid-fluid interfacial area with decreasing contact angles, as would be expected, which is reflected in the experimental measurements of the weakly oil-wet polyethylene bead pack and the moderately water-wet glass bead pack. A rough estimation by visual inspection from these curves would suggest that the contact angles of the glass and polyethylene bead packs are near $\theta \approx 70^\circ$ and $\theta \approx 58^\circ$, respectively. However, we cannot make a quantitative comparison of model and experimental results without knowledge of the experimental contact angles. In general, the LB simulations capture the trends of the relationship between saturation and interfacial fluid-fluid areas. The LB simulations also agree with the trends of the experimental measurements of the fractional fluid-solid interfacial areas, as shown in Figure 3. The fractional nonwetting phase interfacial area decreases with decreasing contact angles, this is a result of the wetting phase dominating occupation of the smaller pore spaces and forcing the nonwetting phase into the largest pores where its fractional interface with the solid decreases. This relationship affects the fraction of a solid surface that is in contact with a wettability altering fluid, and also the location of the fluid in the pore space (i.e., the small pores where clay minerals or organics may be found, or the large pores where multiple mineral constituents may be found.)

3.2. Pore Radius and Fluid Distribution

The pore radius is the maximum radius of a sphere that can occupy a pore. To determine the pore radius distribution, a "sphere packing" of sequentially smaller spheres are packed into the pore space using a limited maximum inscribed sphere approach. First, the voxels of the pore space are labeled with their distance to the pore wall. The labeled pore space is then searched for voxels that fall within a user-defined range (starting with the voxels with the greatest distance from the pore wall). These voxels then become the center of a sphere—with a radius equal to the distance to the closest pore wall—placed in the pore space, and all voxels of the pore space that fall within this sphere are labeled as belonging to the pore radius. Those voxels that are labeled are precluded from seeding new spheres; this is different from the straightforward maximum inscribed sphere approach, for

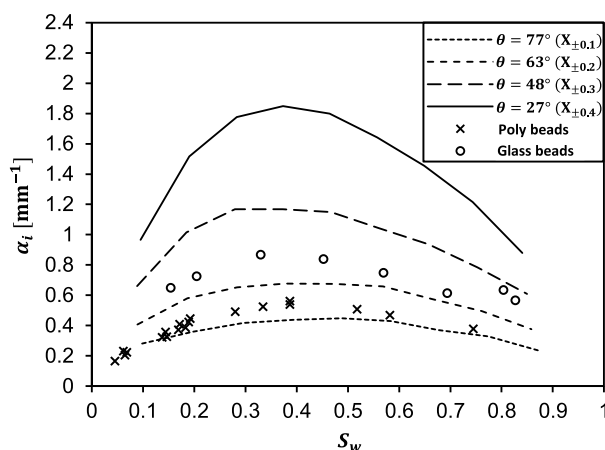


Figure 2. Specific fluid-fluid interfacial areas as a function of wetting phase saturation for the LB simulations and experimental CMT images.

distribution and fluid distribution are presented in Figure 5. We can see from the fluid distribution that decreasing the contact angle pushes the nonwetting phase into the larger pores, and due to the increasing affinity of the wetting phase for the solid surfaces, the wetting phase dominates the smaller pore spaces.

3.3. Two-Phase Flow in a Circular Pore

To test our model against a known semianalytical solution for two-phase immiscible flow, we simulate flow in a circular pore. Two-phase immiscible flow is commonly described using an empirical extension of Darcy's law,

$$v_{\sigma} = \frac{k_a k_{r\sigma}}{\mu_{\sigma}} \nabla P \quad (15)$$

where the mean velocity of each fluid parallel to the direction of flow, v_{σ} , is a function of the dynamic viscosity, μ_{σ} , pressure gradient, ∇P , absolute or single-phase permeability, k_a , and the relative permeability defined as $k_{r\sigma} = k_{e\sigma}/k_a$, where $k_{e\sigma}$ is the effective permeability. In a circular pore

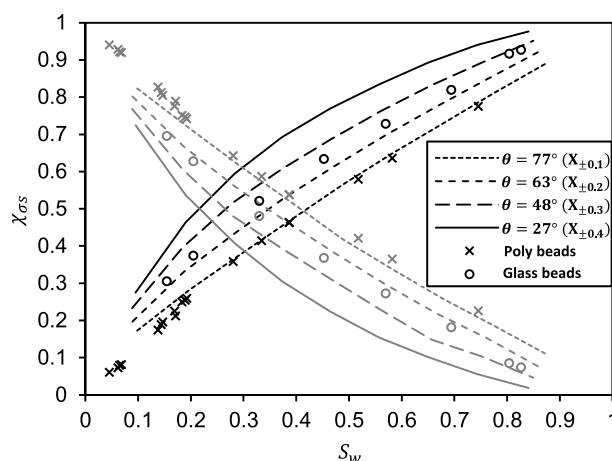


Figure 3. Fractional fluid-solid interfacial areas as a function of wetting phase saturation for the LB simulations and experimental CMT images, the wetting fluid-solid interfacial areas are shown in black and the nonwetting fluid-solid interfacial areas are shown in gray.

which all voxels are considered for seeding of sequentially smaller spheres. Due to the complex nature of pore space, it cannot be completely described by a collection of spheres, such that voxels close to the pore walls are left unlabeled with a pore radius. To complete the description of the pore space, these unlabeled voxels are labeled with the pore radius of the nearest labeled voxels (Figure 4). The pore radius distribution can then be determined by simply summing the labeled voxels. The fluid distribution can also be easily measured by masking the segmented fluid occupation ($\varphi_{\sigma}(\mathbf{x})$) with the pore radius-labeled pore space. The pore radius

where the wetting fluid is distributed as an annulus along the walls of the pore and the viscosity ratio is one, the wetting phase relative permeability is a function of the wetting phase saturation, $k_{rw} = S_w^2$, and the nonwetting phase relative permeability is a function of nonwetting phase saturation, $k_{rnw} = 2S_{nw} + S_{nw}^2/2$. To simulate two-phase flow in a circular pore at varying saturations, the wetting phase fluid is initially distributed as an annulus along the pore walls with the nonwetting phase fluid occupying the nodes in the center in correlation with the desired saturation. The walls of the pore are strongly wetting to maintain the annular distribution of the wetting phase.

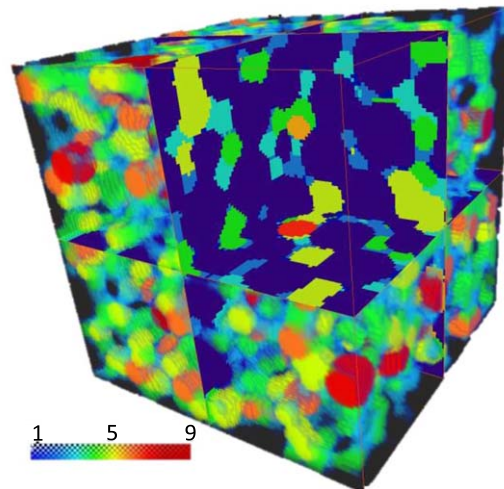


Figure 4. 3-D image and cross-section of pore radius distribution determined by the limited maximum inscribed radius method described in section 3.2. A pore radius is assigned to each fluid voxel (node in LB simulations), and shown here in voxel units (lu in LB simulations).

Otherwise, under weakly wetting conditions, the wetting phase will separate and lose its annular shape, the annular shape being an assumption of the semianalytical solution of immiscible two-phase flow in a circular pore. To determine the relative permeability of fluids in the LB simulation, the momentum in the direction of flow of each fluid is summed over all pore nodes at the given wetting phase saturations,

$$M_{\sigma}(S_{\sigma}) = \sum_x \rho_{\sigma} u_{\sigma}, \quad (16)$$

and normalized to the fully saturated momentum,

$$k_{r\sigma} = \frac{M_{\sigma}(S_{\sigma})}{M_{\sigma}(S_{\sigma}=1)}. \quad (17)$$

To impose concurrent flow in a circular pore with a radius of 11 nodes, an exterior force of $\mathbf{F}_{\text{ext},\sigma} = 0.00001$ is applied to both fluids, and periodic boundaries are imposed at the inlet and outlet. The system is considered to have reached steady state when the convergence criteria were met,

$$\varepsilon > \left(\sqrt{\frac{M_{\sigma}(t-10000) - M_{\sigma}(t)}{M_{\sigma}(t)}} \right)^2. \quad (18)$$

A choice of $\varepsilon = 10^{-3}$ was chosen, based on numerical experiments. Figure 6 shows the results of the LB simulation and the semianalytical solutions for two-phase flow in a circular pore. The difference between the semianalytical solution and the LB simulations is due to the discrete nature of the rendering of the circular pore and the resolution. Previous investigations have shown multicomponent LB models are increasingly more accurate with finer resolutions [Ramstad et al., 2010].

3.4. Relative Permeability

The relative permeability of the porous media is determined by LB simulations in the same manner as described in the section 3.3. However, as was described in Martys and Chen [1996], the total momentum of the fluids did not display a linear relationship with exterior forcing below $N_{Ca} < 10^{-4}$. To determine the relative permeability, exterior forces between $0.0001 \leq F_{\text{ext},\sigma} \leq 0.001$ ($\mu u \times lu / tu^2$) were used. The relative permeability curves for the initial homogenous-wet porous media are shown in Figure 7. At low wetting phase saturations, the nonwetting phase relative permeability exceeds one and the wetting phase relative

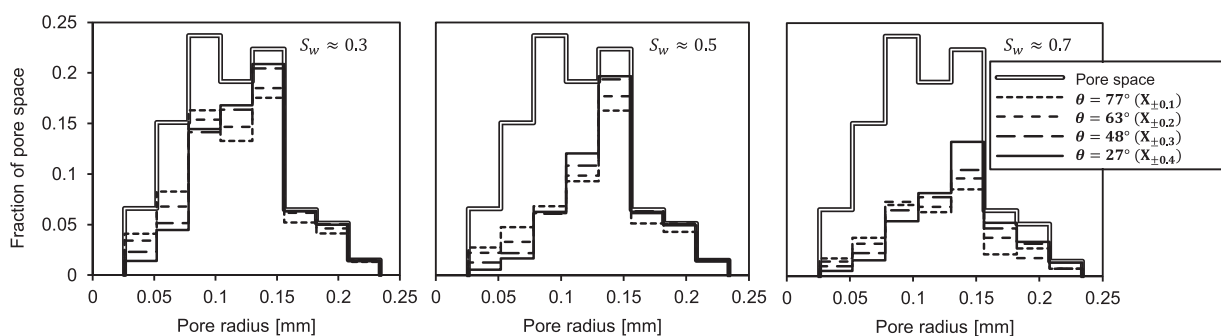


Figure 5. Pore radius (compound lines) and nonwetting phase fluid distribution of initial homogenous-wet states at $S_w \approx 0.3, 0.5, 0.7$. Note: $0.026 \text{ mm} = \text{voxel resolution}$, the binning of the histograms is equal to 1 voxel.

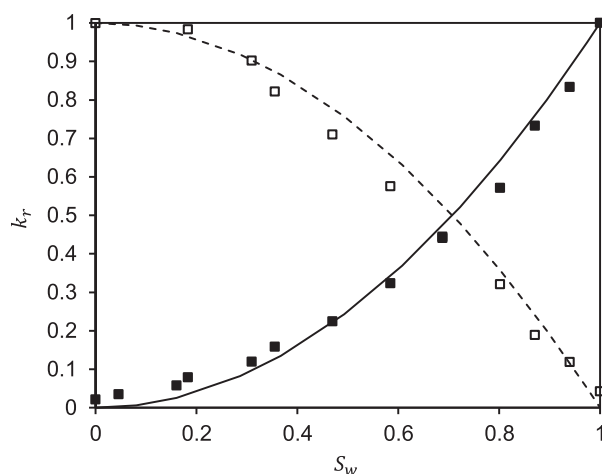


Figure 6. Relative permeability in a circular pore with radius = 11 μ ; LB simulation results (wetting: close squares, nonwetting: open squares) and semi-analytical solution curves (wetting: solid line, nonwetting: dotted line).

permeability is slightly negative. This has also been reported in the preliminary results of Boek and Venturoli [2010]. These values are likely a result of applying periodic boundary conditions to a nonperiodic porous medium. Also, the saturations where these values occur are at or below experimentally observed irreducible wetting phase saturations of $S_w \approx 0.2$ and $S_w \approx 0.08$ for the glass and polyethylene beads respectively, and are unlikely to occur in capillary-dominated displacement processes. We are able to measure the relative permeability at these saturations using the LB simulations due to the employment of a steady state setup which allows for any initial saturation. However, some of these simulations may not have a physical corollary.

Generally, Figure 7 shows decreasing the contact angle also decreases the relative permeability of both phases at all saturations. The variation is small due to the high porosity and connectivity of the pore space. As would be expected, the crossover point for the relative permeability curves occurs at $S_w \approx 0.6$. The relative permeability of the fluids is governed by two competing mechanisms that act to inhibit and promote fluid flow, namely, fluid-solid interfacial area and connectivity, respectively. Greater fluid-solid interfacial area leads to greater resistance to flow, while increased connectivity leads to greater mobility. The dominant factor being the connectivity of the phase, which results in the general trend of increasing phase relative permeability with increasing phase saturation. Unlike the fluid-solid interfacial area, we do not have a simple method of measuring the connectivity of a fluid phase, but given that we have measurements of the solid-fluid interfacial areas we can infer differences in relative permeability that cannot be attributed to trends in the solid-fluid interfacial areas are a result of connectivity. Also the connectivity correlates with the fluid distribution, with the more connected wetting phase occupying smaller pores, as was shown in Figure 5. Thus, connectivity generally increases the relative permeability of a phase with increasing phase saturation, however, for the wetting phase this connectivity also pins it to the smaller pore spaces resulting in a generally lower relative permeability for the wetting phase over the nonwetting phase.

How the wetting phase and nonwetting phase respond to these competing mechanisms can be very different. In Figure 7, we can see the net effect on the nonwetting phase relative permeability is an overall

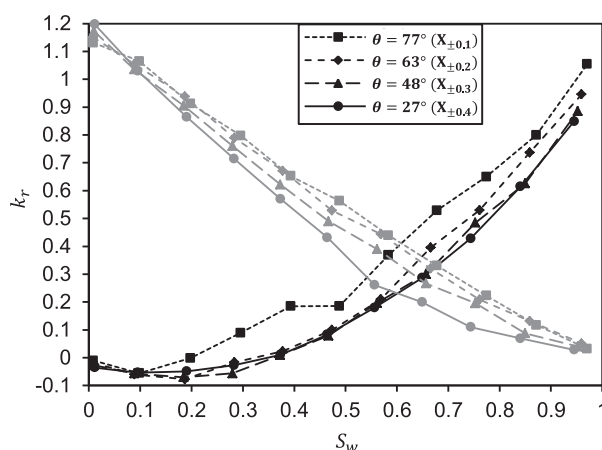


Figure 7. Relative permeability determined by LB simulations for the initial homogenous-wet states. The relative permeability of the wetting and nonwetting phase are shown in black and gray, respectively.

decrease as the fluids become more disconnected (occupy larger pores). Although there is less fluid-solid interfacial area, this effect is dominated by the decrease in connectivity. Unlike the nonwetting phase, the wetting phase relative permeability shows very little dependence on the wetting strength of the porous medium for $\theta < 63^\circ$. There is no decrease in the connectivity of the wetting phase with decreasing contact angles, thus the small decrease in relative permeability with decreasing contact angle can only be attributed to an increase in fluid-solid interfacial areas and increased pinning to smaller pore spaces. It is not surprising that the nonwetting phase relative permeability is

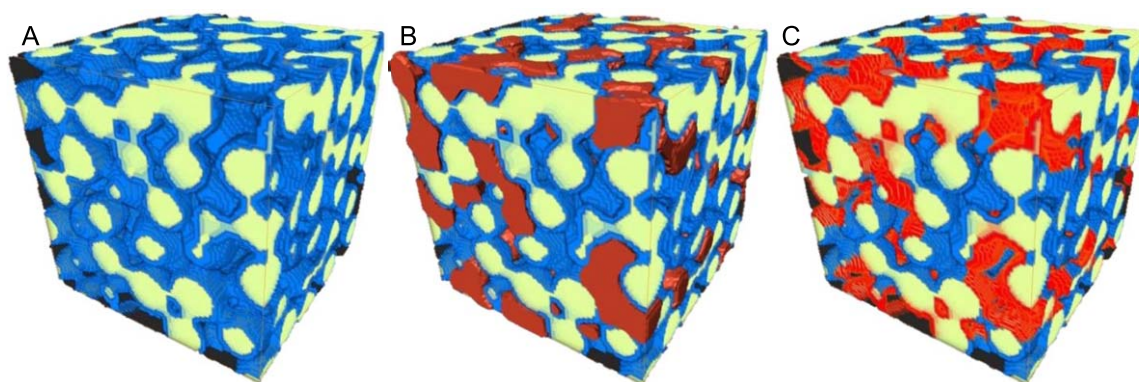


Figure 8. (a) Images of the LB lattice with initial homogenous wettability, (b) the fluid distribution of the nonwetting phase at the end of the simulation of the initial homogenous wettability with $\theta=77^\circ$ and $S_w \approx 0.5$, and (c) the alteration of the adsorption coefficient of the nodes in contact with the nonwetting fluid. This image also summarizes the three parameters determining the mixed-wet state, initial wettability (Figure 8a), saturation of alteration (Figure 8b), and severity of alteration (Figure 8c).

more greatly influenced by its connectivity, being the less connected phase, and the wetting phase relative permeability is more greatly influenced by the fluid-solid interfacial area and pinning to smaller pore spaces, being the generally more well-connected phase. However, regarding the nonwetting phase relative permeability, a similar previous investigation reported the opposite effect from what is reported here. *Li et al.* [2005] simulated two-phase flow in a homogenous sphere pack using a multiple-relaxation-time Shan-Chen type multicomponent LB model and reported an increase in the nonwetting phase relative permeability for strongly wet states ($\theta=25^\circ$) over neutrally wet states ($\theta=65^\circ$). This could be attributed to differences in the pore space geometry resulting in the prevalence of increased nonwetting phase mobility due to the decrease in solid-fluid interfacial area, over the decrease in mobility associated with decreased connectivity as was observed here. The homogenous sphere pack used by *Li et al.* [2005] may have a generally narrower distribution of pore radii, meaning fewer large pore spaces for the nonwetting phase to occupy, increasing the dependence of the nonwetting phase relative permeability on the solid-fluid interfacial area. The interaction of these competing mechanisms is sensitive to small differences in pore space geometry. In the mixed-wet states, individual pores can have mixed-wettability resulting in the competition of these mechanisms within each pore.

3.5. Relative Permeability of Mixed-Wet States

As was previously stated, the adsorption coefficient of the nodes in contact with the nonwetting phase after fluid distribution is established in the homogenous-wet simulations are altered to create a mixed-wet porous medium (Figure 8). The mixed-wet state is the result of three parameters, the initial homogenous-wettability, the saturation at which alteration takes place, and the severity of alteration. Here we will alter the wettability of each of four homogenous-wetting states at a wetting phase saturation near 0.5, with four increasingly severe alterations, resulting in 16 mixed-wet states. The $G_{ads,\sigma}$ of nodes in contact with the nonwetting phase are altered to preferentially wet the nonwetting phase with contact angles $\theta=90^\circ, 103^\circ, 117^\circ, 132^\circ$ ($G_{ads,\sigma}=\mp 0.0, \mp 0.1, \mp 0.2, \mp 0.3$). To avoid confusion, the initial wetting phase is from here on referred to as the wetting phase of the mixed-wet states, and used as the wetting phase saturation in figures. Also, the mixed-wet states will be referred to according to the following indexing, X_m^n , where m is the $G_{ads,\sigma}$ for the initial wettability, and n is the $G_{ads,\sigma}$ for the altered wettability (i.e., $X_{\mp 0.2}^{\mp 0.1}$ would refer to a state that was initially $-G_{ads,w}=G_{ads,nw}=0.2$ wet, then altered as previously stated to $-G_{ads,w}=G_{ads,nw}=-0.1$). The initial homogenous-wet states will use the same indexing as the mixed-wet states absent a superscript.

There are numerous mixed-wet states that could be considered using this framework, we limit this investigation to studying the mixed-wet state resulting at $S_w \approx 0.5$. These mixed-wet states are the result of wettability alteration of the homogenous-wet states at $S_w \approx 0.5$, and therefore the mixed-wet states are dependent on the fluid distribution of the phases at this saturation. The wetting phase at this saturation is described as occupying the smaller pore spaces (Figure 5), and is the more connected phase. Thus, the surfaces altered by the nonwetting phase are disconnected, with an increasing fraction of the surface altered (increasing fractional solid-fluid interfacial area) with increasing contact angle.

The relative permeability curves, fractional solid-fluid interfacial areas and fluid distributions for the mixed-wet states are shown in Figure 9. Recapping the observations of the homogenous-wet states, the nonwetting phase relative permeability was found to decrease with decreasing contact angle due to decreasing connectivity, while the wetting phase relative permeability was found to decrease slightly with decreasing contact angle due to increasing solid-fluid interfacial area and pinning to smaller pore spaces. In general, the wettability alteration has little effect on the wetting phase relative permeability; this was also observed in the work of Hazlett *et al.* [1998]. The fractional wetting phase solid-fluid interfacial areas of the mixed-wet states are generally lower than those of the mixed-wet states. Unlike in the homogenous-wet states, this decrease does not correlate with an increase of the wetting phase relative permeability. We can conclude that any differences in the wetting phase relative permeability of mixed-wet states cannot be attributed to differences in the solid-fluid interfacial area. Instead, the insensitivity of the wetting phase relative permeability to wettability alteration can be attributed to the fluid distribution of the wetting phase at the saturation of alteration. At $S_w \approx 0.5$, the wetting phase has developed a well-connected pathway (occupies smaller pores and has a high fractional solid-fluid interfacial area). The solid in contact with the wetting phase remains unaltered; thus, this connected path remains in the mixed-wet states. This is reflected in the fluid distributions shown in Figure 9; the wetting phase remains the dominant phase occupying the smaller pore spaces. For the $X_{\pm 0.1}^n$ mixed-wet states, there is some decrease in the wetting phase relative permeability observed for the $X_{\pm 0.1}^{n0.3}$ mixed-wet state. This decrease in wetting phase relative permeability is limited to the $X_{\pm 0.1}^n$ mixed-wet state as a result of its poorer connectivity of the established unaltered wetting phase pathways in comparison to those of the $X_{\pm 0.2}^n$, $X_{\pm 0.3}^n$, and $X_{\pm 0.4}^n$ mixed-wet states. But even this small decrease only exists for a mixed-wet state suffering a severe alteration. Overall, the wetting phase relative permeability is unaffected by the wettability alteration; the established unaltered wetting phase pathways that encourage the wetting phase to occupy the smaller pores dominate the mobility of the wetting phase.

The nonwetting phase relative permeability is significantly decreased in the mixed-wet states, and as in the case of the wetting phase, the most dramatic effect is seen for the $X_{\pm 0.1}^n$ mixed-wet states. The same decrease in relative permeability for the nonwetting phase in mixed-wet states was found in the work of Hazlett *et al.* [1998]. For the $X_{\pm 0.2}^n$, $X_{\pm 0.3}^n$, and $X_{\pm 0.4}^n$ mixed-wet states the severity of the wettability alteration has little effect on the relative permeability of the nonwetting phase, but the existence of a wettability alteration does. The altered solid surfaces are no longer dominated by the initial wetting phase, resulting in an increase of the nonwetting phase fluid-solid interfacial area. The decrease in the nonwetting phase relative permeability correlates with an increase in the nonwetting phase fluid-solid interfacial area, but not proportionately. Particularly for the $X_{\pm 0.1}^n$ mixed-wet states, the decrease in the nonwetting phase relative permeability cannot be attributed to the increases in fluid-solid interfacial area alone. In general, for all of the mixed-wet states, the nonwetting phase becomes pinned by its affinity to these altered solid surfaces, such that the wetting phase is now competing for occupation of the larger pore spaces. This pinning and competition result in a “squeezing” of the nonwetting phase between the wetting phase occupied small pore spaces and the wetting phase competing for the larger pore spaces. This is reflected in the resulting fluid distributions shown in Figure 9. The nonwetting phase increasingly occupies smaller pore spaces in the mixed-wet states. The relative permeability of the nonwetting phase for the $X_{\pm 0.1}^n$ mixed-wet states responds to the severity of alteration because the distribution of the altered surfaces includes fewer of the smaller pore spaces. Thus, there is less of a squeezing effect, and a more general competition for the smaller pore spaces. Therefore, with increasing severity of alteration the nonwetting phase occupies a larger portion of the smaller pore spaces, resulting in a decrease of the nonwetting phase relative permeability.

Had the wettability alteration occurred at high wetting phase saturations, we would expect the same result to a lesser extent, simply due to the fact that less of the solid surface would be altered. Wettability alteration at lower wetting phase saturations would have a somewhat increasing effect, however, not as much as one may at first think. The extreme example of altering the entire surface when fully saturated with the nonwetting phase would result in a simple role reversal of the wetting and nonwetting phases. This would suggest that at lower wetting phase saturations of wettability alteration, we could expect the wetting phase relative permeability to “rebound” and begin to respond with increasing mobility. However, saturations below irreducible wetting phase saturation are unlikely to occur. At saturations near the irreducible wetting phase saturation, the wetting phase will continue to dominate the smaller pore spaces. And as occurred in our

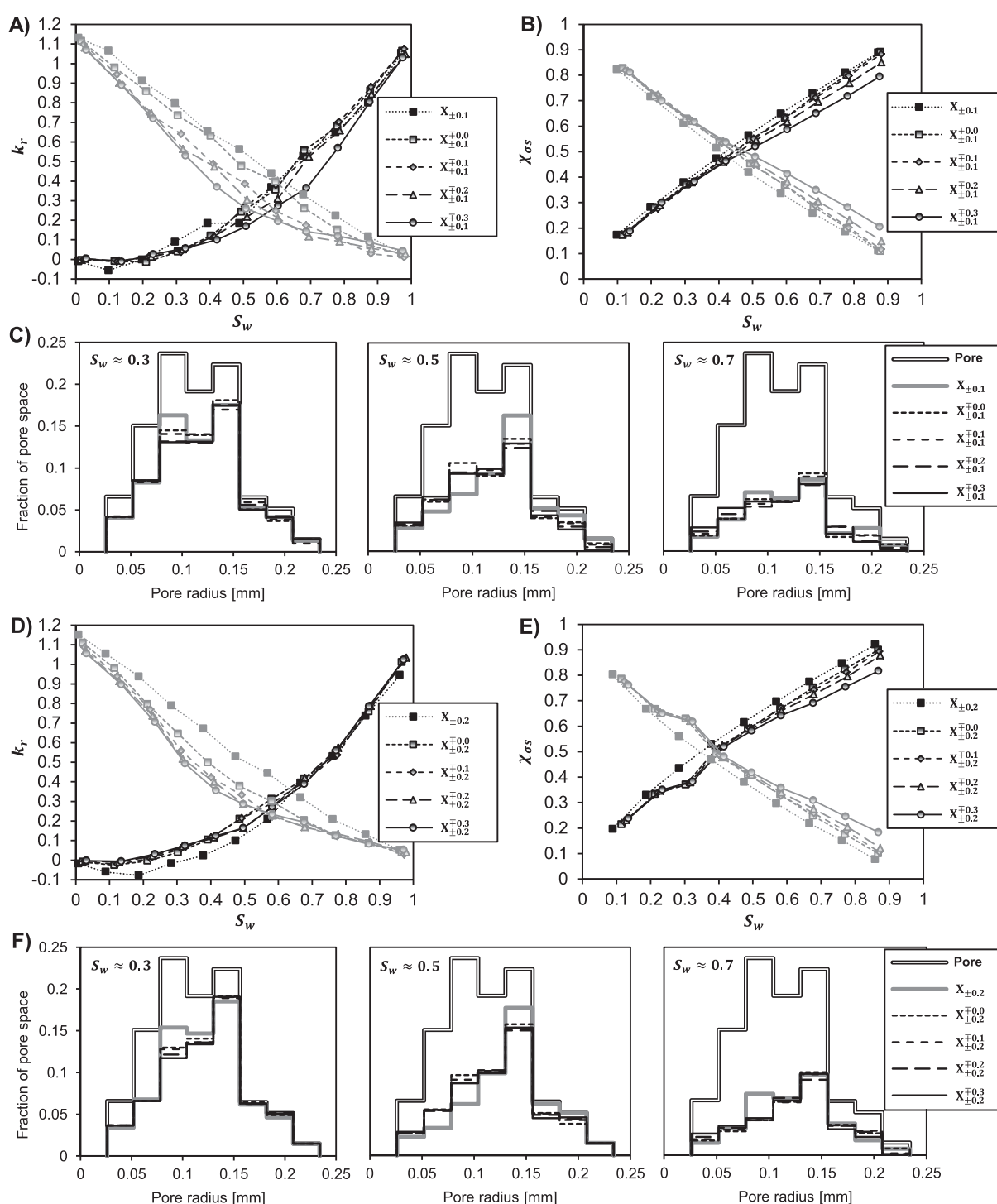


Figure 9. Relative permeability, fractional fluid-solid interfacial areas, and fluid distributions determined by LB simulations for the mixed-wet states of the originally homogenous-wet states, (a–c) $\theta=77^\circ$ ($X_{\pm 0.1}$), (d–f) $\theta=63^\circ$ ($X_{\pm 0.2}$), (g–i) $\theta=48^\circ$ ($X_{\pm 0.3}$), and (j–l) $\theta=27^\circ$ ($X_{\pm 0.4}$), with increasing severity of alteration. The relative permeability and fractional fluid-solid interfacial areas of the wetting and nonwetting phase are shown in black and gray, respectively.

simulations, wettability alteration will not occur in these smaller pore spaces. The wetting phase in the mixed-wet states will continue to be pinned to these smaller pore spaces, and generally will not experience any increase in relative permeability, as one might intuitively expect when considering the extreme example of the entire surface being altered. At these saturations the nonwetting phase relative permeability will be slightly more affected than what we see here at $S_w \approx 0.5$; however, we do not predict significant differences.

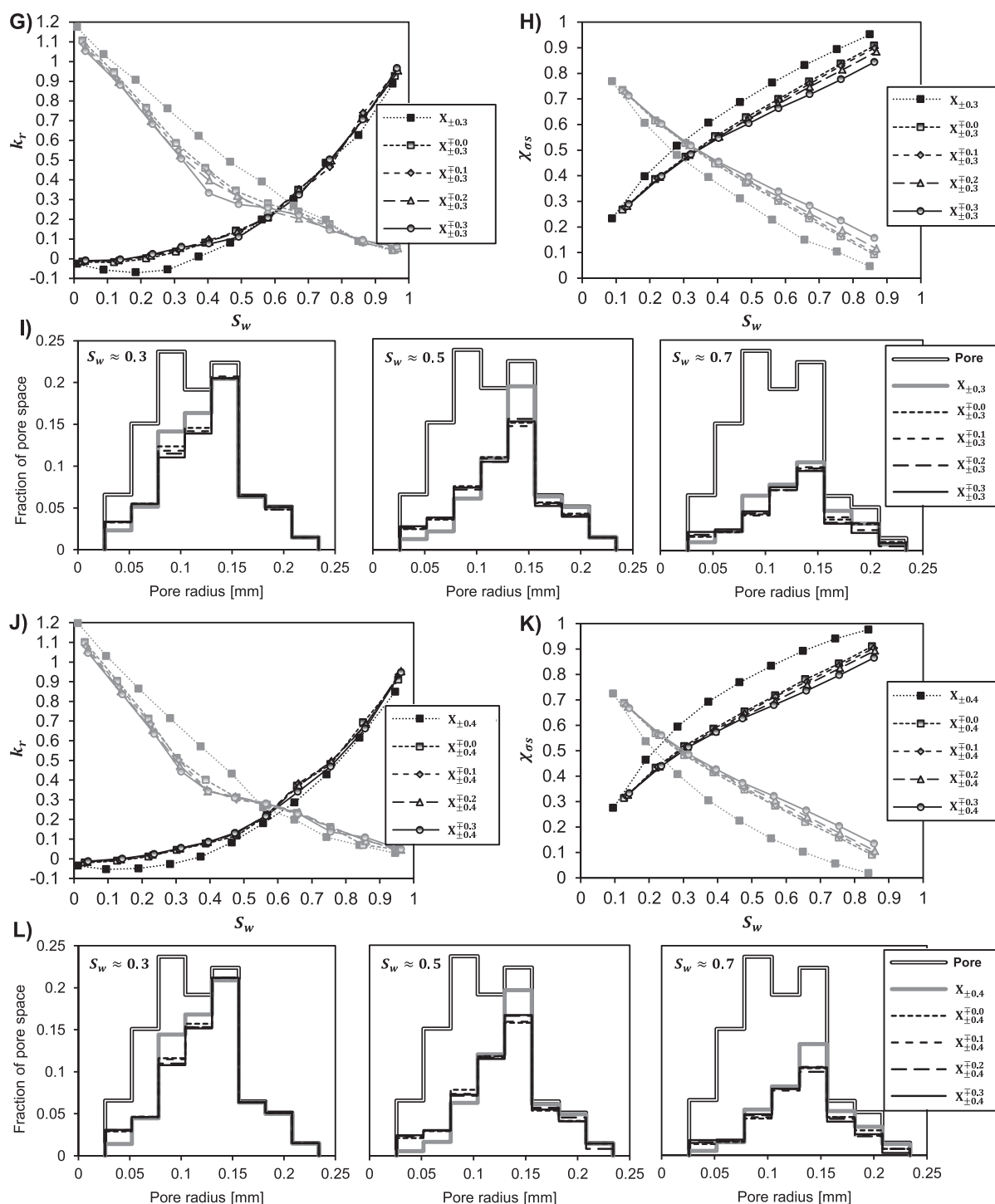


Figure 9. (continued)

In our simulations of mixed-wet states, the nonwetting phase relative permeability has been significantly decreased by the wettability alteration. There is very little nonwetting phase mobility left to be lost.

Comparable studies to this one are limited for the most part to numerical experiments using pore-network modeling. There are a few notable differences between PNMs and LB models. As was described in the background section, pore-network models use networks of capillary tube elements to represent the pore space topology, while LB models use direct translations of CMT images to construct the lattice. This also means

that wetting films are simulated by very different means. In PNMs, the wetting phase is simulated as thin films, allowing for very low wetting phase saturations to maintain connectivity. Consequently, in mixed-wet scenarios it is possible for a pore to contain a thin film of one phase sandwiched between the other phase occupying the center and corners of the pore [Blunt, 1997]. The wetting phase films in a lattice Boltzmann simulation are limited in their thickness to the resolution of the lattice, and may or may not appear depending on the resolution of the lattice and the strength of the adsorption coefficient ($G_{ads,\sigma}$) used. Also PNMs simulate displacements, unlike here, where our simulations are steady state. The PNM study of mixed-wettability in six different types of limestone of Gharbi and Blunt [2012] offers a plausible comparison to this work. They investigated the mixed-wet states of PNMs constructed from CMT images of limestone cores. They also found a significant reduction in the nonwetting phase (oil) relative permeability for wettability alteration fractions of 0.25 and 0.5—similar to solid surface fractions altered at $S_w \approx 0.5$ here. However, they also report a significant reduction in the wetting phase relative permeability, not seen here. This can be attributed to not only differences in the pore space geometry, but also the method in which fluid films are simulated. At $S_w \approx 0.5$, our wetting phase remains well connected for homogenous-wet states $X_{\pm 0.2}$, $X_{\pm 0.3}$, and $X_{\pm 0.4}$, and as was previously stated there remains a well-connected unaltered solid-surface for the wetting-phase to be established, ensuring an insignificant effect on the wetting phase relative permeability for the mixed-wet states. In the mixed-wet states of Gharbi and Blunt [2012], much of the wetting phase existed as thin films, resulting in very low wetting phase permeability. The inability to simulate fluid films beyond the resolution of the lattice can make comparisons between pore-network model results and those seen here difficult when thin films determine fluid mobility.

4. Conclusions

We have presented a study of the dependence of relative permeability on wettability for both homogenous-wet and mixed-wet porous media using LB modeling. Comparison between LB simulation and experimental results show the LB simulations capture the trends of experimentally observed fluid-fluid and fluid-solid interfacial areas. Since our mixed-wet states were created by altering the wettability of the solid in contact with the nonwetting phase, it is important that these interfacial areas are accurately predicted by the LB model, thus ensuring realistic mixed-wet states.

The homogenous-wet states displayed a decrease in relative permeability for both phases with decreasing contact angles. This is attributed here to the competition of two mechanisms affecting fluid flow. With decreasing contact angle, the nonwetting phase becomes more disconnected and occupies larger pore spaces. This occupation results in less nonwetting fluid-solid interfacial areas which could increase the relative permeability of the nonwetting phase; however, the decreasing connectivity dominates this effect resulting in lower nonwetting phase relative permeability. The slight decrease in the wetting phase relative permeability with decreasing contact angle is in part a result of greater fluid-solid interfacial area, but more significantly the pinning of the wetting phase to the smaller pore spaces.

The pores of the mixed-wet state are themselves mixed, and the interaction between the two competing mechanisms controlling flow will also compete within individual pores. In this investigation, we find that the connectivity and distribution of the wetting phase at the saturation of wettability alteration (or vice-versa the lack of connectivity of the nonwetting phase) is critical to the significance of the effect the alteration to a mixed-wet state will have on the fluid mobility. In general, the severity of alteration is inconsequential for the wetting phase relative permeability, given the unaltered solid surface is well connected. When this unaltered surface is not as well-connected, as is the case for the originally weakly wet case ($\theta = 77^\circ$), a severe alteration can result in some decrease of the wetting phase relative permeability. The nonwetting phase relative permeability, in general, is significantly decreased by the alteration to a mixed-wet state. Interestingly, given the unaltered solid surface is well connected, the severity of the alteration is inconsequential; however, the existence of a mixed-wet state significantly decreases the relative permeability, including when the alteration is to neutrally wet. The decrease of the nonwetting phase relative permeability is attributed to a “squeezing” of the nonwetting phase between the wetting-phase dominated small pores and the wetting phase competition for altered large pores, resulting in a pushing of the nonwetting phase into smaller pore spaces. When the unaltered surface is not well connected, as is the case for the originally weakly wet case ($\theta = 77^\circ$), an increasing severity of alteration leads to proportionally decreasing nonwetting phase relative permeability. This decrease is not proportional to increasing nonwetting fluid-solid

interfacial areas, and can be attributed to a more general competition for smaller pores. Here we only investigated alteration at $S_w \approx 0.5$. The response to a wettability alteration at $S_w > 0.5$ would be comparable to the results we see here to a lesser extent, due to less of the solid surface being altered. At lower wetting phase saturations, we would also expect results very similar to those seen here, due to the pinning of the wetting phase to the smaller pore spaces.

The framework presented here to study wettability alteration and its effect on the relative permeability of two-phase flow in a simple porous medium can be applied to natural consolidated and unconsolidated porous media. Our initial wettability states are homogenous; for natural porous media, the initial wettability will be determined by the mineral constituents and their locations in the pore space geometry. We present simulations of varying alteration severity. For natural porous media, the level of wettability alteration is a result of complex fluid-mineral interactions and would likely require bulk studies of wettability alteration for individual mineral constituents. Given that the wettability of individual mineral constituents can be determined, LB simulations can be adopted to estimate fluid flow properties, such as relative permeability, for a wide assortment of scenarios. However, it is important to note that natural porous media generally possess far more complex pore space geometries than what has been presented here, and subsequently the lattices required to capture this complexity may be substantially larger. Increases in the lattice size can greatly increase the computational demand of LB simulations, which may become computationally prohibitive.

Acknowledgments

This material is based upon work supported by the National Science Foundation under grant 0747585.

References

- Al-Futaisi, A., and T. W. Patzek (2004), Secondary imbibition in NAPL-invaded mixed-wet sediments, *J. Contam. Hydrol.*, **74**, 61–81, doi:10.1016/j.jconhyd.2004.02.005.
- Al-Raoush, R. I. (2009), Impact of wettability on pore-scale characteristics of residual nonaqueous phase liquids, *Environ. Sci. Technol.*, **43**, 4796–4801, doi:10.1021/es802566s.
- Boek, E. S., and M. Venturoli (2010), Lattice-Boltzmann studies of fluid flow in porous media with realistic rock geometries, *Comput. Math. Appl.*, **59**, 2305–2314, doi:10.1016/j.camwa.2009.08.063.
- Blunt, M. J. (1997), Effects of heterogeneity and wetting on relative permeability using pore level modeling, *SPE J.*, **2**(1), 70–87, doi:10.2118/36762-PA.
- Blunt, M. J., M. D. Jackson, M. Piri, and P. H. Valvatne (2002), Detailed physics, predictive capabilities and macroscopic consequences for pore network models of multiphase flow, *Adv. Water Resour.*, **25**, 1069–1089, doi:10.1016/S0309-1708(02)00049-0.
- Brusseau, M. L., S. Peng, G. Schnaar, and M. S. Constanza-Robinson (2006), Relationships among air-water interfacial area, capillary pressure, and water saturation for a sandy porous medium, *Water Resour. Res.*, **42**, W03501, doi:10.1029/2005WR004058.
- Brusseau, M. L., H. Janousek, A. Murao, and G. Schnaar (2008), Synchrotron X-ray microtomography and interfacial partitioning tracer test measurements of NAPL-water interfacial areas, *Water Resour. Res.*, **44**, W01411, doi:10.1029/2006WR005517.
- Buckley, J. S., and Y. Liu (1998), Some mechanisms of crude oil/brine/solid interactions, *J. Petrol. Sci. Eng.*, **20**, 155–180, doi:10.2118/37230-PA.
- Coles, M. E., R. D. Hazlett, P. Spanne, W. E. Soll, E. L. Muegge and K. W. Jones (1998), Pore level imaging of fluid transport using synchrotron X-ray microtomography, *J. Petrol. Sci. Eng.*, **19**, 55–63, doi:10.1016/S0920-4105(97)00035-1.
- Constanza-Robinson, M. S., K. H. Harrold, and R. M. Lieb-Lappen (2008), X-ray microtomography determination of air-water interfacial area-water saturation relationships in sandy porous media, *Environ. Sci. Technol.*, **42**, 2949–2956, doi:10.1021/es072080d.
- Culligan, K. A., D. Wildenschild, B. S. B. Christensen, W. G. Gray, and M. L. Rivers (2006), Pore-scale characteristics of multiphase flow in porous media: A comparison of air-water and oil-water experiments, *Adv. Water Resour.*, **29**, 227–238, doi:10.1016/j.advwatres.2005.03.021.
- Dalla, E., M. Hilpert, and C. T. Miller (2002), Computation of the interfacial area for two-fluid porous medium systems, *J. Contam. Hydrol.*, **56**, 25–48, doi:10.1016/S0169-7722(01)00202-9.
- Dixit, A. B., S. R. McDougall, and K. S. Sorbie (1998), A pore-level investigation of relative permeability hysteresis in water-wet systems, *SPE J.*, **3**(2), 115–123, doi:10.2118/37233-PA.
- Dixit, A. B., S. R. McDougall, K. S. Sorbie, and J. S. Buckley (1999), Pore-scale modeling of wettability effects and their influence on oil recovery, *SPE Reservoir Eval. Eng.*, **2**, 25–36, doi:10.2118/54454-PA.
- Flowkit Ltd. (2012), Palabos. [Available at <http://www.palabos.org/>]
- Gharbi, O., and M. J. Blunt (2012), The impact of wettability and connectivity on relative permeability in carbonates: A pore network modeling analysis, *Water Resour. Res.*, **48**, W12513, doi:10.1029/2012WR011877.
- Ghassemi, A., and A. Pak (2011), Numerical study of factors influencing relative permeabilities of two immiscible fluids flowing through porous media using lattice Boltzmann method, *J. Petrol. Sci. Eng.*, **77**, 135–145, doi:10.1016/j.petrol.2011.02.007.
- Hao, L., and P. Cheng (2010), Pore-scale simulations on relative permeabilities of porous media by lattice Boltzmann method, *Int. J. Heat Mass Transfer*, **53**, 1908–1913, doi:10.1016/j.ijheatmasstransfer.2009.12.066.
- Hazlett, R. D. (1995) Simulation of capillary-dominated displacements in microtomographic images of reservoir rocks, *Transp. Porous Media.*, **20**(1–2), 21–35, doi:10.1007/BF00616924.
- Hazlett, R. D., S. Y. Chen, and W. E. Soll (1998), Wettability and rate effects on immiscible displacement: Lattice Boltzmann simulation in microtomographic images of reservoir rocks, *J. Petrol. Sci. Eng.*, **20**, 167–175, doi:10.1016/S0920-4015(98)00017-5.
- He, X. Y., Q. S. Zuo, L. S. Luo, and M. Dembo (1997), Analytic solutions of simple flows and analysis of nonslip boundary conditions for the lattice Boltzmann BGK model, *J. Stat. Phys.*, **87**(1–2), 115–136, doi: 10.1007/BF02181482.
- Hoiland, L. K., K. Spildo, and A. Skauge (2007), Fluid flow properties for different classes of intermediate wettability as studied by network modeling, *Transp. Porous Media.*, **70**, 127–146, doi:10.1007/s11242-006-9088-x.
- Huang, H., D. T. Thorne, M. G. Schaap, and M. C. Sukop (2007), Proposed approximation for contact angles in Shan-and-Chen-type multi-component multiphase lattice Boltzmann models, *Phys. Rev. E*, **76**, 066701, doi:10.1103/PhysRevE.76.066701.

- Hui, M., and M. J. Blunt (2000), Effects of wettability on three-phase flow in porous media. *J. Phys. Chem. B*, **104**, 3833–3845, doi:10.1021/jp9933222.
- Iglauer, S., A. Paluszny, C. H. Pentland, and M. J. Blunt (2011), Residual CO₂ imaged with X-ray microtomography, *Geophys. Res. Lett.*, **38**, L21403, doi:10.1029/2011GL049680.
- Jackson, M. D., P. H. Valvatne, and M. J. Blunt (2003), Prediction of wettability variation and its impact on flow using pore- to reservoir-scale simulations, *J. Petrol. Sci. Eng.*, **39**, 231–246, doi:10.1016/S0920-4105(03)00065-2.
- Jadhunandan, P. P., and N. R. Morrow (1995), Effect of wettability on waterflood recovery for crude-oil/brine/rock systems, *SPE Reservoir Eng.*, **10**(1), 40–46, doi:10.2118/22597-PA.
- Jerauld, G. R., and J. J. Rathmell (1997), Wettability and relative permeability of Prudhoe Bay: A case study in mixed-wet reservoirs. *SPE Reservoir Eng.*, **12**(1), 58–65, doi:10.2118/28576-PA.
- Joekar-Niasar, V., S. M. Hassanizadeh, and A. Leijnse (2008), Insights into the relationships among capillary pressure, saturation, interfacial area and relative permeability using pore network modeling, *Transp. Porous Media*, **74**, 201–219, doi:10.1007/s11242-007-9191-7.
- Kovscek, A. R., H. Wong, and C. J. Radke (1993), A pore-level scenario for the development of mixed wettability in oil reservoirs, *AIChE J.*, **39**(6), 1072–1085, doi:10.1002/aic.690390616.
- Kumar, M., A. Fogden, T. Senden, and M. Knackstedt (2012), Investigation of pore-scale mixed wettability, *SPE J.*, **17**(1), 20–30, doi:10.2118/129974-PA.
- Landry, C. J., Z. T. Karpyn, and M. Piri (2011), Pore-scale analysis of trapped immiscible fluid structures and fluid interfacial areas in oil-wet and water-wet bead packs, *Geofluids*, **11**, 209–227, doi:10.1111/j.1468-8123.2011.00333.x.
- Lebedeva, E. V., and A. Fogden (2011), Micro-CT and wettability analysis of oil recovery from sandpacks and the effect of waterflood salinity and kaolinite, *Energy Fuel*, **25**, 5683–5694, doi:10.1021/ef201242s.
- Li, H., C. Pan, and C. T. Miller (2005), Pore-scale investigation of viscous coupling effects for two-phase flow in porous media, *Phys. Rev. E*, **72**, 026705, doi:10.1103/PhysRevE.72.026705.
- Martys, N. S., and H. Chen (1996), Simulation of multicomponent fluids in complex three-dimensional geometries by the lattice Boltzmann method, *Phys. Rev. E*, **53**(1), 743–750, doi:10.1103/PhysRevE.53.743.
- Mukherjee, P. P., C. Y. Wang, and Q. Kang (2009), Mesoscopic modeling of two-phase behavior and flooding phenomena in polymer electrolyte fuel cells, *Electro. Acta*, **54**, 6861–6875, doi:10.1016/j.electacta.2009.06.066.
- Oren, P. E., and S. Bakke (2003), Reconstruction of Berea sandstone and pore-scale modeling of wettability effects, *J. Petrol. Sci. Eng.*, **39**, 177–199, doi:10.1016/S0920-4105(03)00062-7.
- Oren, P. E., S. Bakke, and O. J. Arntzen (1998), Extending predictive capabilities to network models, *SPE J.*, **3**(4), 324–336, doi:10.2118/52052-PA.
- Pan, C., M. Hilpert, and C. T. Miller (2004), Lattice-Boltzmann simulation of two-phase flow in porous media, *Water Resour. Res.*, **40**, W01501, doi:10.1029/2003WR002120.
- Pan, C., L. S. Luo, and C. T. Miller (2006), An evaluation of lattice Boltzmann schemes for porous medium flow simulation, *Comput. Fluids*, **35**, 898–909, doi:10.1016/j.compfluid.2005.03.008.
- Porter, M. L., M. G. Schaap, and D. Wildenschild (2009), Lattice-Boltzmann simulations of the capillary pressure-saturation-interfacial area relationship for porous media, *Adv. Water Resour.*, **32**, 1632–1640, doi:10.1016/j.advwatres.2009.08.009.
- Prodanovic, M., W. B. Lindquist, and R. S. Seright (2006), Porous structure and fluid partitioning in polyethylene cores from 3D x-ray microtomographic imaging, *J. Colloid Interface Sci.*, **298**, 282–297, doi:10.1016/j.jcis.2005.11.053.
- Prodanovic, M., W. B. Lindquist, and R. S. Seright (2007), 3D image-based characterization of fluid displacement in a Berea core, *Adv. Water Resour.*, **30**, 214–226, doi:10.1016/j.advwatres.2005.05.015.
- Qian, Y. H., D. d'Humieres, and P. Lallemand (1992), Lattice BGK models for Navier-Stokes equations, *Europhys. Lett.*, **17**(6), 479–484, doi:10.1209/0295-5075/17/6/001.
- Ramstad, T., P. E. Oren, and S. Bakke (2010), Simulation of two-phase flow in reservoir rocks using a lattice Boltzmann method, *SPE J.*, **15**(4), 917–927, doi:10.2118/124617-PA.
- Ramstad, T., N. Idnani, C. Nardi, and P. E. Oren (2012), Relative permeability calculations from two-phase flow simulations directly on digital images of porous rock, *Transp. Porous Media*, **94**, 487–504, doi:10.1007/s11242-011-9877-8.
- Reeves, P. C., and M. A. Celia (1996), A functional relationship between capillary pressure, saturation, and interfacial area as revealed by a pore-scale network model, *Water Resour. Res.*, **32**(8), 2345–2358, doi:10.1029/96WR01105.
- Robin, M., E. Rosenberg, and O. Fassi-Fihri (1995), Wettability studies at the pore level: A new approach by use of cryo-SEM, *SPE Form. Eval.*, **10**(1), 11–19, doi:10.2118/22596-PA.
- Saraji, S., L. Goual, and M. Piri (2010), Adsorption of asphaltenes in porous media under flow conditions, *Energy Fuel*, **26**, 6009–6017, doi:10.1021/ef100881k.
- Schaap, M. G., M. L. Porter, B. S. B. Christensen, and D. Wildenschild (2007), Comparison of pressure-saturation characteristics derived from computed tomography and lattice Boltzmann simulations, *Water Resour. Res.*, **43**, W12506, doi:10.1029/2003WR002120.
- Shan, X., and H. Chen (1993), Lattice Boltzmann model for simulating flows with multiple phases and components, *Phys. Rev. E*, **47**(3), 1815–1819, doi:10.1103/PhysRevE.47.115.
- Shan, X., and H. Chen (1994), Simulation of nonideal gases and liquid-gas phase transitions by the lattice Boltzmann equation, *Phys. Rev. E*, **49**(4), 2941–2948, doi:10.1103/PhysRevE.49.2941.
- Silin, D., L. Tomatsu, S. M. Benson, and T. W. Patzek (2011), Microtomography and pore-scale modeling of two-phase fluid distribution, *Transp. Porous Media*, **86**, 495–515, doi:10.1007/s11242-010-9636-2.
- Sukop, M. C., H. Huang, L. L. Chen, M. D. Deo, K. Oh, and J. D. Miller (2008), Distribution of multiphase fluids in porous media: Comparison between lattice Boltzmann modeling and micro-x-ray tomography, *Phys. Rev. E*, **77**, 026710, doi:10.1103/PhysRevE.77.026710.
- Turner, M. L., L. Knufing, C. H. Arns, A. Sakellariou, T. J. Senden, A. P. Sheppard, R. M. Sok, A. Limaye, W. V. Pinczewski, and M. A. Knackstedt (2004), Three-dimensional imaging of multiphase flow in porous media, *Physica A*, **339**, 166–172, doi:10.1016/j.physa.2004.03.05.
- Vogel, H. J., J. Tolke, V. P. Schulz, M. Krafczyk, and K. Roth (2005), Comparison of a Lattice-Boltzmann model, a full-morphology model, and a pore network model for determining capillary pressure-saturation relationships, *Vadose Zone J.*, **4**, 380–388, doi:10.2136/vzj2004.0114.
- Zhao, X., M. J. Blunt, and J. Yao (2010), Pore-scale modeling: Effects of wettability on waterflood oil recovery, *J. Petrol. Sci. Eng.*, **71**, 169–178, doi:10.1016/j.petrol.2010.01.011.